



**HAL**  
open science

# Crystallographic texture and velocities of ultrasonic waves in a Ni-based superalloy manufactured by laser powder bed fusion

Amal Khabouchi, Pascal Ventura, Nicolas Leymarie, Alain Hazotte, Lionel Germain

► **To cite this version:**

Amal Khabouchi, Pascal Ventura, Nicolas Leymarie, Alain Hazotte, Lionel Germain. Crystallographic texture and velocities of ultrasonic waves in a Ni-based superalloy manufactured by laser powder bed fusion. *Materials Characterization*, 2020, 169, pp.110607. 10.1016/j.matchar.2020.110607. hal-03118300

**HAL Id: hal-03118300**

**<https://hal.univ-lorraine.fr/hal-03118300>**

Submitted on 22 Sep 2022

**HAL** is a multi-disciplinary open access archive for the deposit and dissemination of scientific research documents, whether they are published or not. The documents may come from teaching and research institutions in France or abroad, or from public or private research centers.

L'archive ouverte pluridisciplinaire **HAL**, est destinée au dépôt et à la diffusion de documents scientifiques de niveau recherche, publiés ou non, émanant des établissements d'enseignement et de recherche français ou étrangers, des laboratoires publics ou privés.



Distributed under a Creative Commons Attribution - NonCommercial 4.0 International License

# Crystallographic texture and velocities of ultrasonic waves in a Ni-based superalloy manufactured by laser powder bed fusion

Amal Khabouchi<sup>1</sup>, Pascal Ventura<sup>1</sup>, Nicolas Leymarie<sup>3</sup>, Alain Hazotte<sup>1,2</sup>, Lionel Germain<sup>1,2</sup>

<sup>1</sup> Laboratoire d'Étude des Microstructures et de Mécanique des Matériaux, Université de Lorraine, CNRS, Arts et Métiers Paris Tech, LEM3, F-57000, Metz, France

<sup>2</sup> Laboratory of Excellence on Design of Alloy Metals for Low-mAss Structures (DAMAS), Université de Lorraine, France

<sup>3</sup> Department of Nondestructive Testing, CEA LIST, Gif-sur-Yvette 91191, France

## Abstract

This study investigated the mechanisms of formation of the microstructure and texture of an Inconel 625 manufactured by additive manufacturing, using laser-based powder bed fusion. The resulting texture has a quadratic symmetry and a composite organization of grains. Some elongated grains have their  $\langle 100 \rangle$  aligned along the build-up direction and grow from the middle of the melt pool, whereas the others are inclined with a lower texture. This is explained on the basis of usual solidification mechanisms. The overall texture is not very pronounced (texture index of 1.24) but sufficient to influence ultrasound wave propagation in a measurable manner. The difference is the most pronounced between the slow and fast quasi transverse waves. The contribution of two main factors influencing the anisotropy, namely the anisotropy of the single crystal and the shape of the grains, are discussed in the paper.

**Keywords:** Additive manufacturing; Inconel 625; texture; anisotropy; Ultrasonic waves; EBSD

## 1. Introduction

Additive manufacturing (AM) of metallic parts is one of the main emerging process technologies in recent years [1]. First applications mostly concern components with high added value and rather low batch size. For instance, some components with complex geometries made of Ni-based superalloys are already produced for high-temperature aeronautic or aerospace applications. In this field, laser-based powder-bed fusion (L-PBF) is the mostly used technique [2,3]. During the last decade, R&D on additive manufacturing of metallic parts logically focused on achieving –with reproducibility– parts with high density and mechanical properties comparable to parts made by standard processes [4–6]. Direct relationships were empirically established between process parameters and macroscopic properties, whereas less attention was paid to microstructures resulting from the deposition process [7]. This lack of interest was partly justified by the fact that the microstructure can be modified by solid phase transformations during cooling or by subsequent heat treatments. As-manufactured L-PBF microstructures are known to present rather low and fine chemical segregations, due to rapid solidification [8–12]. Rapid cooling also generally leads to a lower proportion of strengthening phases [13]. However, these phases are homogeneously distributed and their optimal volume fraction can be adjusted afterwards by heat treatment. Both these microstructure features appear favorable for mechanical properties. Actually, the main microstructural drawback associated with AM is the possible anisotropy resulting from directional manufacturing. As far as L-PBF is concerned, a lot of works pointed out a more or less strong difference between mechanical properties measured parallel or perpendicular to the building direction [7,14,15]. However, it is not always clear if this mechanical anisotropy results from the porosities or impurities leaved between successive laser melting pools and/or from the crystallographic texture induced by the multi-pass solidification process.

Texture strongly depends on the deposition process, on the laser beam properties (power and energy distribution) and on the building strategy (hatching distance, lasing speed and path along and between layers ...) [16–19]. As a result, different crystallographic textures can be obtained [20]. The most common one has large columnar grains with  $\langle 100 \rangle$  crystal axes parallel to the building direction [21] but more recently  $\langle 110 \rangle$  fibers [22,23] and random textures [24] have also been reported. Strong texture is difficult to reduce through heat treatments, especially in the case of metallic alloys which do not encounter solid phase transformations such as Ni-based alloys [25,26]. At the present time, due to the high complexity of AM processes, just a few models exist to predict the texture intensity

of L-PBF parts from the process parameters [27,28]. Therefore, there is a need to understand the development of grains structure during this process.

Crystallographic texture can also affect the characteristics of mechanical waves, through the introduction of elastic anisotropy in the material [29]. It is known that the wave velocities of compression and shear modes can vary according to their direction of propagation [30]. When using ultrasonic (US) testing methods, strong elastic anisotropy of the tested part can result in an inaccurate detection or location of defects [31–34]. Inversely, various ultrasonic non-destructive evaluation (NDE) techniques can be used in order to determine anisotropic elastic properties [35–38]. In the case of polycrystalline materials, this allows the determination of elastic constants of an equivalent homogeneous medium with respect to the wavelength scale used (around 1 mm at 5 MHz for a metallic alloy).

The main objectives of the present work were to evaluate the magnitude of crystallographic texture resulting from optimized L-PBF processing of Inconel 625 parts and to relate it the anisotropy of US wave velocities. The Ni-based superalloy Inconel 625 was chosen because it is of industrial interest, but also as a model material with a high single-crystal elastic anisotropy and no solid phase transformation which could modified the as-deposited microstructure. The present paper focuses on results obtained on parallelepipeds made by L-PBF conditions. Their resulting microstructure and crystallographic texture were characterized. Their elastic anisotropy was deduced from the measured distribution of crystal orientations, coupled with the knowledge of single-crystal stiffness matrix. This allowed the prediction of the velocities of US waves as a function of AM process direction and comparison with direct measurements.

## 2. Materials and methods

Two similar parallelepipeds ( $60 \times 60 \times 10 \text{ mm}^3$ ) of Inconel 625® alloy were manufactured by Polyshape company via the laser powder bed technique (L-PBF), using optimized but undisclosed process parameters in an EOS® M270 machine. Figure 1 shows a schematic view of one sample to illustrate part of the laser scanning strategy used. Each layer was scanned with the laser direction at  $45^\circ$  from the parallelepiped faces and a rotation of  $90^\circ$  was applied between two successive layers. In the following, the build-up direction is noted Z. X and Y are parallel to others parallelepiped faces and defined the plane perpendicular to the build-up direction. One parallelepiped was used for microstructure and crystallographic texture investigations, while the other was used to measure velocities of the transversal and longitudinal US waves along X, Y and Z axes.

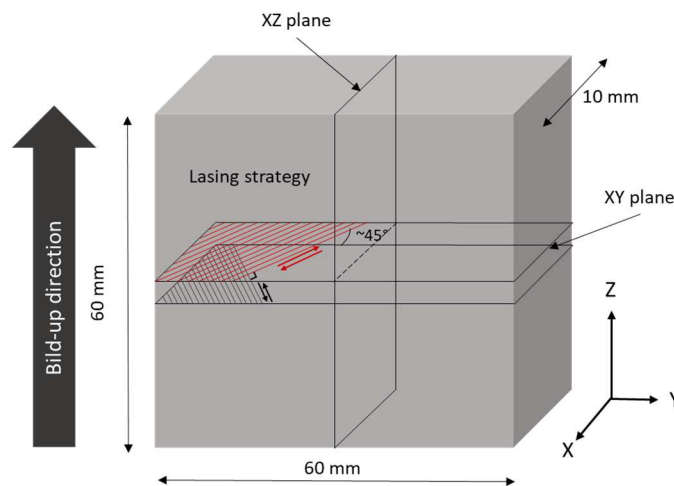


Figure 1. Sample geometry, lasing strategy and observation surfaces

### 2.1. Characterization of microstructure and crystallographic texture

One parallelepiped was cut along two planes perpendicular and parallel to the build-up direction (resp. XY and XZ planes). The microstructure and crystallographic texture of the material were observed at the center of these surfaces, where the deposition process can be considered as stationary [39].

The microstructure was observed using both Optical (OM) and Scanning Electron (SEM) microscopes. Porosities were detected by OM, after conventional polishing with successive SiC papers and a final polishing step with diamond paste (1 $\mu$ m). Quantitative analysis of their size and volume fraction was performed using ImageJ software. Fusion pools were revealed by electrolytic etching in a solution of 48 ml H<sub>2</sub>SO<sub>4</sub>, 40 ml of H<sub>2</sub>NO<sub>3</sub> and 12 ml of H<sub>2</sub>PO<sub>4</sub>, with a 0.5 V voltage during 40 s. Microstructures were also observed by SEM, using both a Zeiss Supra40 SEM with field-emission gun or a JEOL 6490 SEM with tungsten filament. Grain structure was observed with the back scattered electron detector on polished surfaces and from EBSD (Electron Back Scattering Diffraction) maps, while solidification structure was observed after electrolytic etching.

Crystallographic textures were obtained from large EBSD maps of polished surfaces, using JEOL 6490 SEM under an acceleration voltage of 20 kV. A Nordlys S camera from Oxford Instrument coupled with the EBSD indexing software AZtec was used. Only the FCC crystal symmetry was searched, corresponding to both the Ni-rich  $\gamma$  matrix and the fine  $\gamma'$  phase coherent with  $\gamma$  matrix. However, no effort was done in the present work to identify the presence of strengthening phases. The experimental configuration allowed good indexing rate (better than 95%) with an acquisition rate of 70Hz, which enabled to scan large areas in reasonable time. EBSD data were treated afterwards using both Channel5 software from Oxford or ATEX software developed in LEM3 [40]. In the following, the measured textures and microstructures are represented using either pole figures (distribution of the orientations of one crystallographic direction with respect to X, Y and Z sample axes) or orientation maps colored as the inverse pole figures (IPF-maps). In this latter case, the color of a pixel always represents the crystallographic direction parallel to the build-up axis, Z, whatever the analyzed plane. Surfaces of several mm<sup>2</sup> large were investigated along XY and YZ planes, in order to get statistically significant orientation distributions. Grain boundaries were considered having a disorientation larger than 6°. The mean grain sizes along X, Y and Z directions were measured by intercept method on orientation maps.

## 2.2. Elastic anisotropy modeling

The elastic properties (stiffness matrix) of the material were estimated from the distribution of grains orientations and the elastic constants of a single crystal. Concerning Inconel 625 alloy, which has a cubic symmetry, two sets of single-crystal stiffness constants  $C_{11}$ ,  $C_{12}$  and  $C_{44}$  were found in the literature [41,42]. They are reported in Table 1, together with the anisotropy coefficient  $A$  (or Zener ratio) defined as  $2C_{44}/(C_{11}-C_{12})$  [43]. The transition from single- to poly-crystal needs a rule of mixture taking into account the distribution of elastic strain/stress within grains. The two extreme models assume perfect homogeneity of either stress (Reuss scheme) [44] or strain (Voigt scheme) [45] within grains, leading to lower and upper bounds of stiffness, respectively. Several models giving intermediate values have also been proposed. Among them, the Hill scheme [46] is the simplest. It corresponds to the average of Reuss and Voigt and gives a reasonable value in case of equiaxed grains. In the present study, Reuss, Voigt and Hill schemes have been tested with the two sets of single crystal stiffness constants of Table 1. In addition, another set of elastic constants was also estimated to give results closer to US measurements. More details concerning the modeling are given in §. 3.4.

*Table 1. Stiffness coefficients and anisotropy ratio of Inconel 625<sup>®</sup> single crystal*

$C_{11}$ (GPa)	$C_{12}$ (GPa)	$C_{44}$ (GPa)	$A$	Ref.
243.6	156.7	117.8	2.71	[41]
234.6	145.4	126.2	2.83	[42]

## 2.3. Ultrasonic characterization from wave velocity measurements

Velocities of ultrasonic waves along the X, Y and Z axes of the second parallelepiped were measured at CEA-LIST laboratory. Both longitudinal and transverse (or shear) US waves were tested. A classical method was used for longitudinal waves propagation. Velocities of longitudinal waves were deduced from measurements performed on a sample immersed in water, using transducers Olympus V120 with a working frequency of 5 MHz and an aperture of 6.35 mm. More attention was paid to the characterization of transverse US waves propagation which is more

sensitive to elastic anisotropy (Figure 2a). Direct contact transducers Olympus V115 were used in transmission mode, with a working frequency of 5 MHz and an aperture of 6.35 mm. Contact coupling between transducers and sample surfaces was ensured by means of a shear wave couplant. The device allows rotating the parallelepiped around the wave propagation axis (X, Y or Z). In case of an isotropic material, the velocity of an US transverse wave does not depend on the position around the rotation axis. However, in case of an elastic anisotropic material, it depends on both wavefront and polarization (transverse) directions with respect to the anisotropy main axes of the material (see Figure 2b). Considering a material with orthotropic anisotropy (orthogonal symmetry with different elastic moduli along X, Y and Z directions), and assuming that the propagation direction is shared with one axis of orthotropy, the transverse wave properties can be directly deduced according to their polarization directions parallel to the symmetry axes (see discussion in Part.4 for details). In the present study, these two shear waves were detected and their rates were measured. From these measurements, anisotropy factors of US transverse wave, denoted  $\alpha_i$ , is deduced and defined such as:

$$\alpha_i = \left( \frac{|V_{ij} - V_{ik}|}{\text{moy}(V_{ij}; V_{ik})} \right) * 100 \quad (1)$$

where  $i$  is the propagation direction (X, Y, or Z) and  $V_{ij}$  and  $V_{ik}$  are the measured velocities of the quasi-transverse waves decomposed in the two others orthotropic directions ( $i \neq j \neq k$ ). This anisotropy factor was measured in the three directions of the parallelepiped. As explained in § 3.4, it is possible to relate the stiffness matrix coefficients of the polycrystalline anisotropic material to the velocities of longitudinal and transverse waves in different directions, assuming an orthotropic model for elastic anisotropy. Therefore, in the present paper, anisotropy factors  $\alpha_i$  and stiffness coefficients  $C_{ij}$  were directly or indirectly obtained from both texture and US propagation measurements and their values compared.

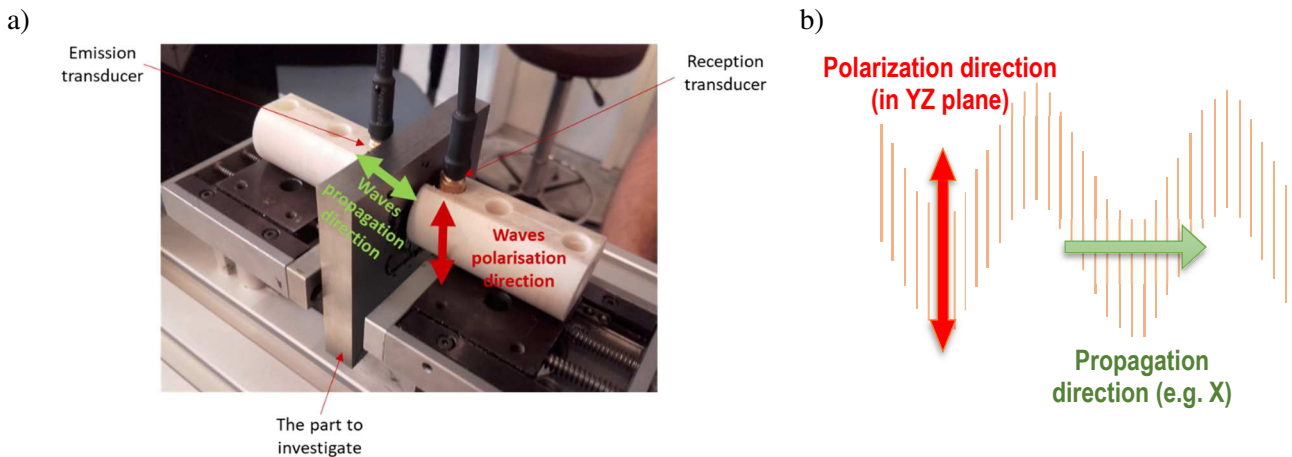


Figure 2. a) Experimental device used for the measurement of velocity of transverse US waves; b) Illustration of the different directions of interest in the propagation analysis (in the example, X is the US propagation direction)

It should be noted that the validity of this characterization method is linked to the nature of the waves considered. In order to determine the mechanical properties of the medium, we have to estimate the velocities of bulk waves corresponding to the solutions of the wave equation for an infinite medium. In practice, this implies that the dimensions of the sample must be large compared to the size of the probe. If along the X axis this condition is clearly verified, this working assumption becomes more questionable according to the other two directions of propagation Y and Z.

### 3. Results

#### 3.1. Microstructure

Figure 3 collects OM and SEM micrographs illustrating the structure of the deposited material observed along both XY and XZ surfaces. Due to the specific lasing strategy, an intricate structure can be seen, with the traces of ex-liquid pools clearly visible. It can be noted that successive pools appear aligned over long distances along the Z

direction (cf. Figure 3.a). Their width and depth are largely dispersed, with their means estimated at about 85  $\mu\text{m}$  and 35  $\mu\text{m}$ , respectively. Porosities are also observed, indicated by arrows in Figure 3 (a and b), but with a very low volume fraction of about 0.2 %, and a mean size of about 10.8  $\mu\text{m}$ . Their shape appears irregular and they are mostly located in between laser traces, which results in alignments parallel to the built-up direction. This suggests that they probably result from a lack of fusion [47]. At a finer scale, the microstructure illustrated at Figure 3.d shows chemical contrast typical from dendritic solidification [48,49], with a mean arm spacing of about 1  $\mu\text{m}$ . No second phase was detected neither by high resolution SEM nor by X Ray diffraction. However, the present paper does not focus on the very fine microstructure but mostly on grain morphology and orientation.

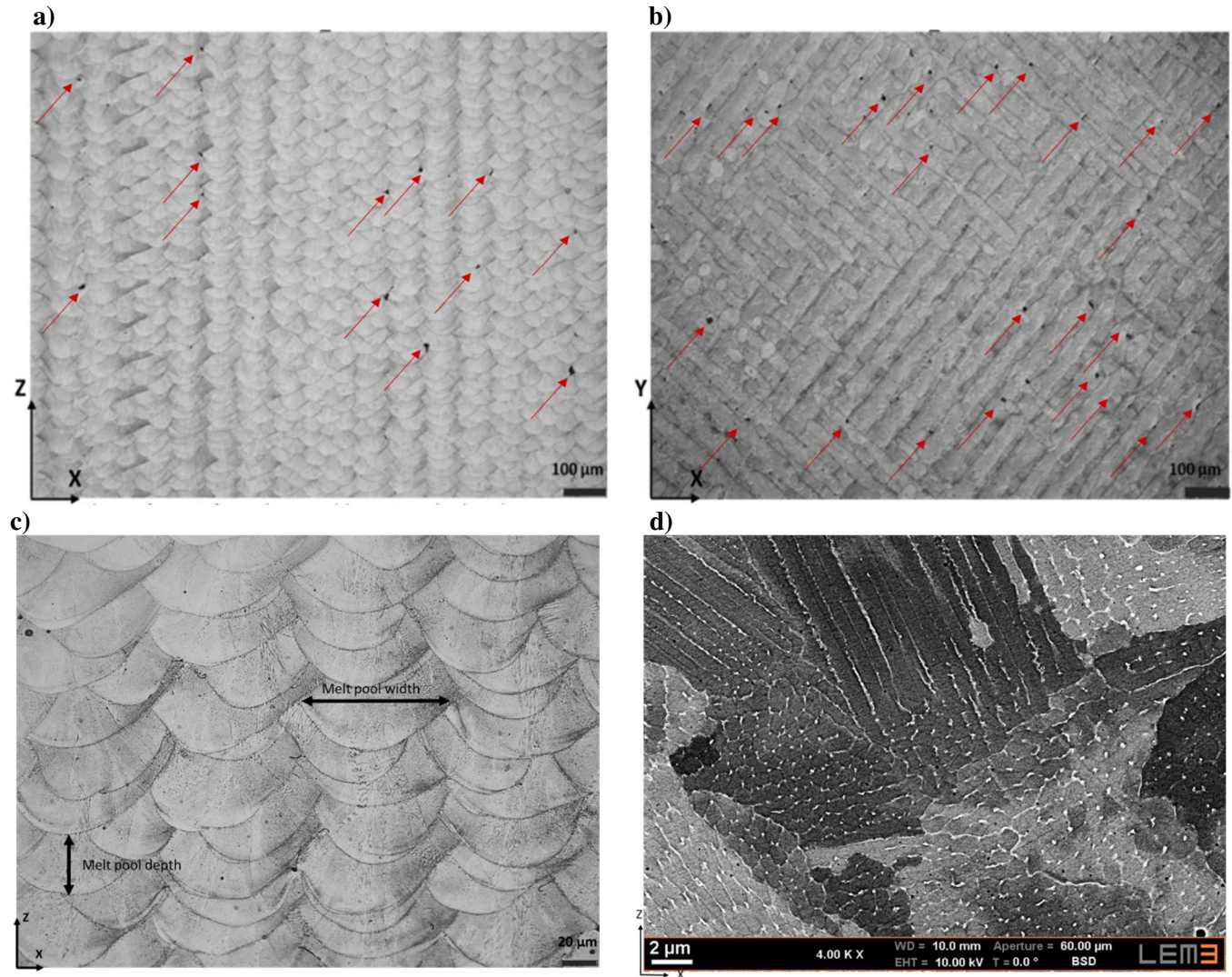


Figure 3. OM and SEM micrographs along XZ (a, b and d) and XY (b) plane: a) and b) traces of laser paths; c) aspect of ex-liquid pools; b) solidification segregation at finer scale

Figure 4 shows a SEM micrograph and an EBSD map illustrating the grain structure of AM alloy. Two different grain morphologies are observed: some grains appear elongated along the build-up direction, whereas the majority of them are shorter with more erratic shapes and a growth direction rather oblique with respect to Z direction. However, as illustrated by Figure 4b, this trend is more or less marked depending on the location. The grain sizes were measured along X (or Y) and Z directions by intercept method on XZ plane. The distance between two measurement lines was about 30  $\mu\text{m}$  and grains with a surface less than 6 pixels were excluded from the analysis to limit the influence of indexation noise. The resulting mean intercept lengths along X and Z directions were found equal to  $\lambda_x=10.1 \mu\text{m}$  and  $\lambda_z=12.7 \mu\text{m}$ , respectively.

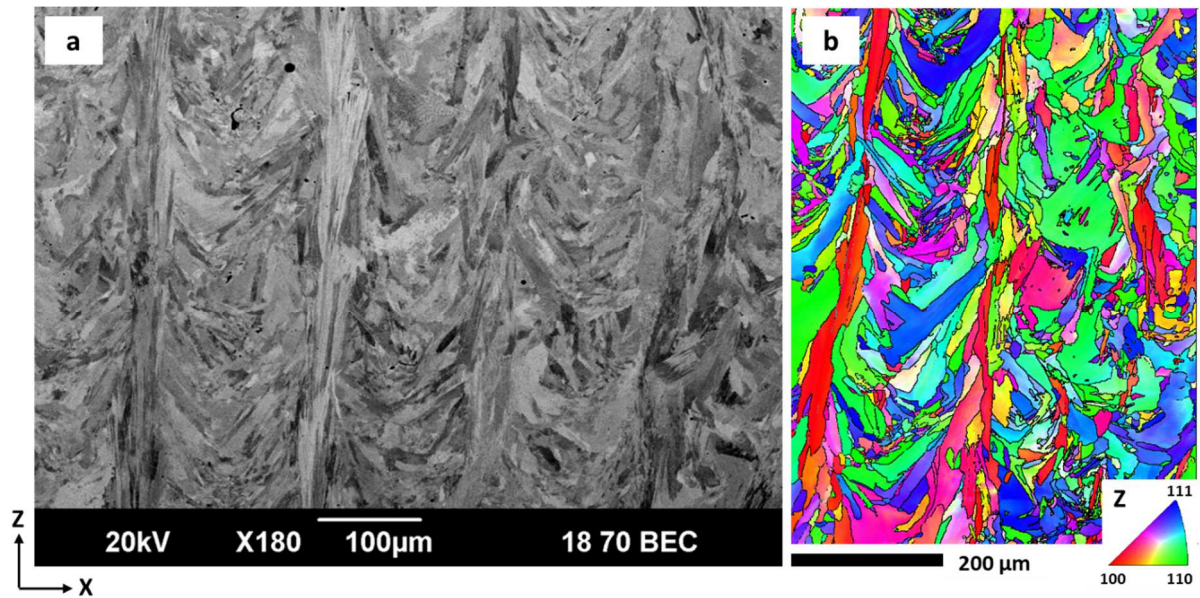


Figure 4. Granular microstructure observed along a XZ surface: a) SEM micrograph (back scattered electrons); b) EBSD map (grain boundaries in black)

The localization of the two morphologies of grains with respect to the melt pools was inferred using hardness indentations as markers (Figure 5). Some of the columnar red grains in the EBSD map are marked with a white line on top of the optical micrograph. It reveals that elongated grains are localized in the middle of successive aligned liquid pools, whereas the other grains (inclined) are present in between. It is also very clear that the main growth direction grains is perpendicular to the melt pool border.

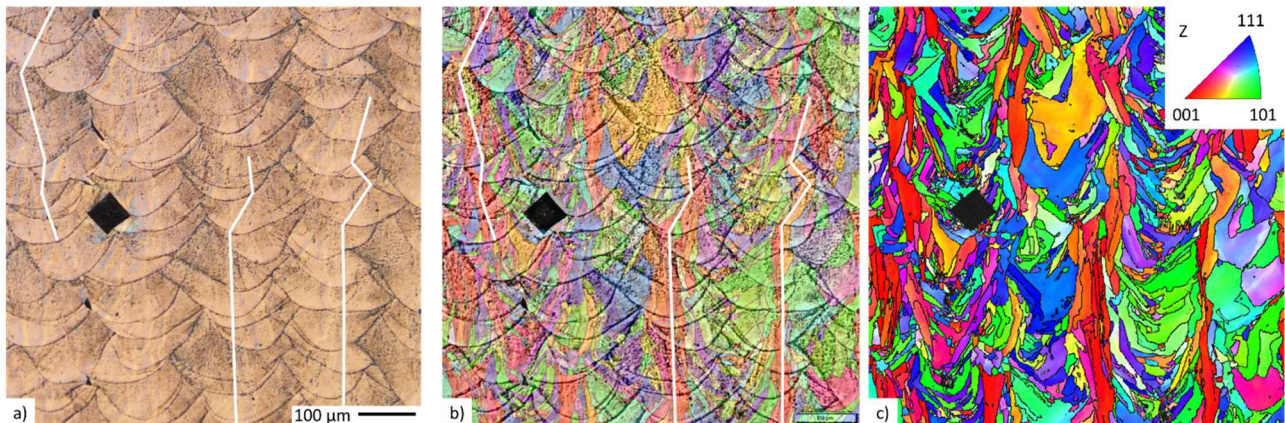


Figure 5: Localization of the elongated grains with respect fusion pools. a) Optical micrograph of the etched sample. Some  $\langle 001 \rangle$  columnar grains have been overlapped with white lines. c) corresponding EBSD. b) Overlap of figure c) with figure a) modified to enhance the contrast of the melt pools.

### 3.2. Crystallographic texture

Figure 6 shows EBSD maps measured along both XY and XZ planes of the parallelepiped, while Figure 7 reports the corresponding  $\{100\}$   $\{110\}$   $\{111\}$  pole figures. The grain morphology and texture distribution are clearly related to the lasing strategy. It is worthwhile to note that, in addition to elongated grains previously detected parallel to the build-up direction (Figure 4b and Figure 6a), a similar development is also observed parallel to the lasing directions (Figure 6b). Most of these elongated grains appear oriented with one  $\langle 100 \rangle$  crystal axis parallel to the Z direction. Globally, the sample texture is relatively low (texture index = 1.24) with a slight reinforcement of  $\langle 100 \rangle$  along the build-up direction Z and at  $45^\circ$  of X/Y directions, i.e. parallel to the lasing directions.

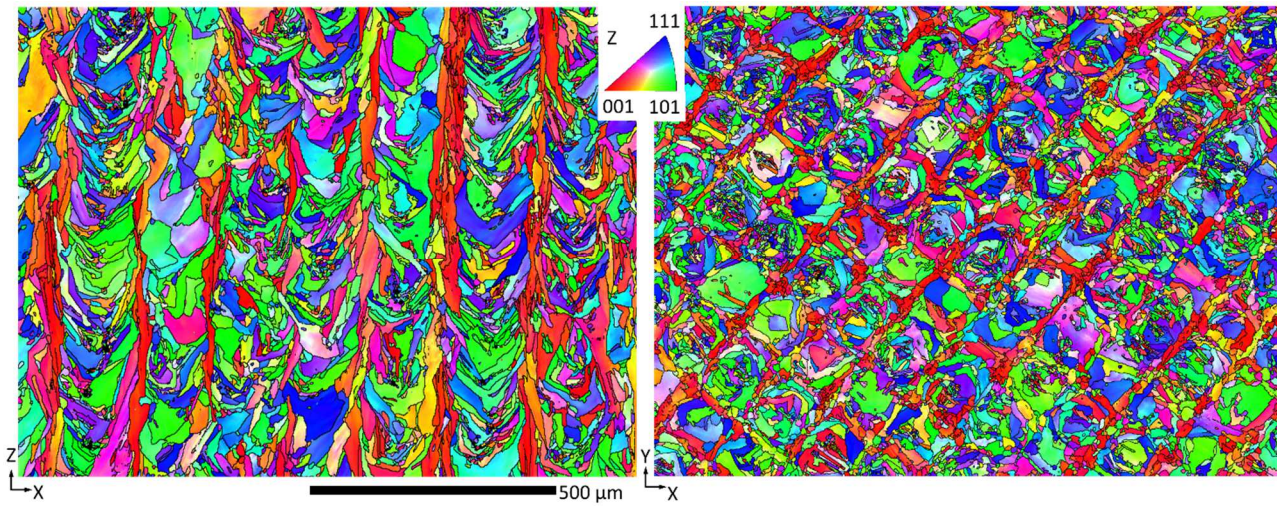


Figure 6 :EBSD IPF maps along XZ and XY planes of the parallelepiped; the triangle gives the correspondence between the colors of pixels and the local crystal direction parallel to the build-up direction Z, Grain boundaries with a disorientation greater than  $6^\circ$  are in black

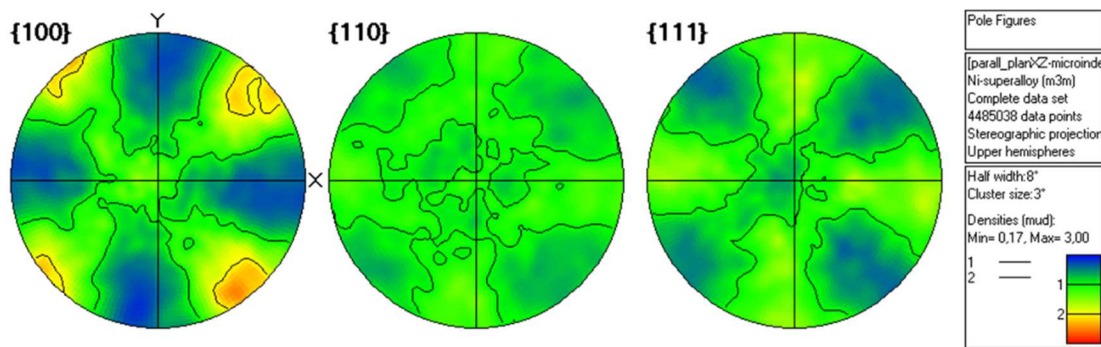


Figure 7. Pole figures reporting the distribution of crystallographic orientations  $\langle 100 \rangle$ ,  $\langle 110 \rangle$  and  $\langle 111 \rangle$  in relation with the X, Y and Z axes of the parallelepiped

To confirm with higher statistics that this specific texture is associated with the development of elongated  $\langle 100 \rangle \parallel Z$  grains, a large EBSD mapping with an area of  $4.2 \times 1.7 \text{ mm}^2$  was performed along a XZ plane (cf. Figure 8a). After detecting the grains, two orientation sets were separated: the first one corresponding to the pixels belonging to elongated grains, i.e. grains with aspect ratio higher than 4 (the aspect ratio being defined as the ratio of the major axis to minor one of the best fitting ellipse), and the second one being the complementary set. EBSD maps and  $\{100\}$  pole figures are given at Figure 8b and Figure 8c for these two sets. From this analysis, it is clear that the slight texture detected on the whole sample is mostly due to the elongated grains located in the middle of melt pools as they represent a fraction of 25% of the volume. The texture of the complementary set is close to random and, remarkably, present little  $\langle 100 \rangle$  density in the Z direction. Instead, the  $\{110\}$  pole figure (not shown here) has a slight reinforcement in that Z direction. The mechanism behind this resulting microstructure is discussed in §.4, on the basis of solidifications mechanisms.

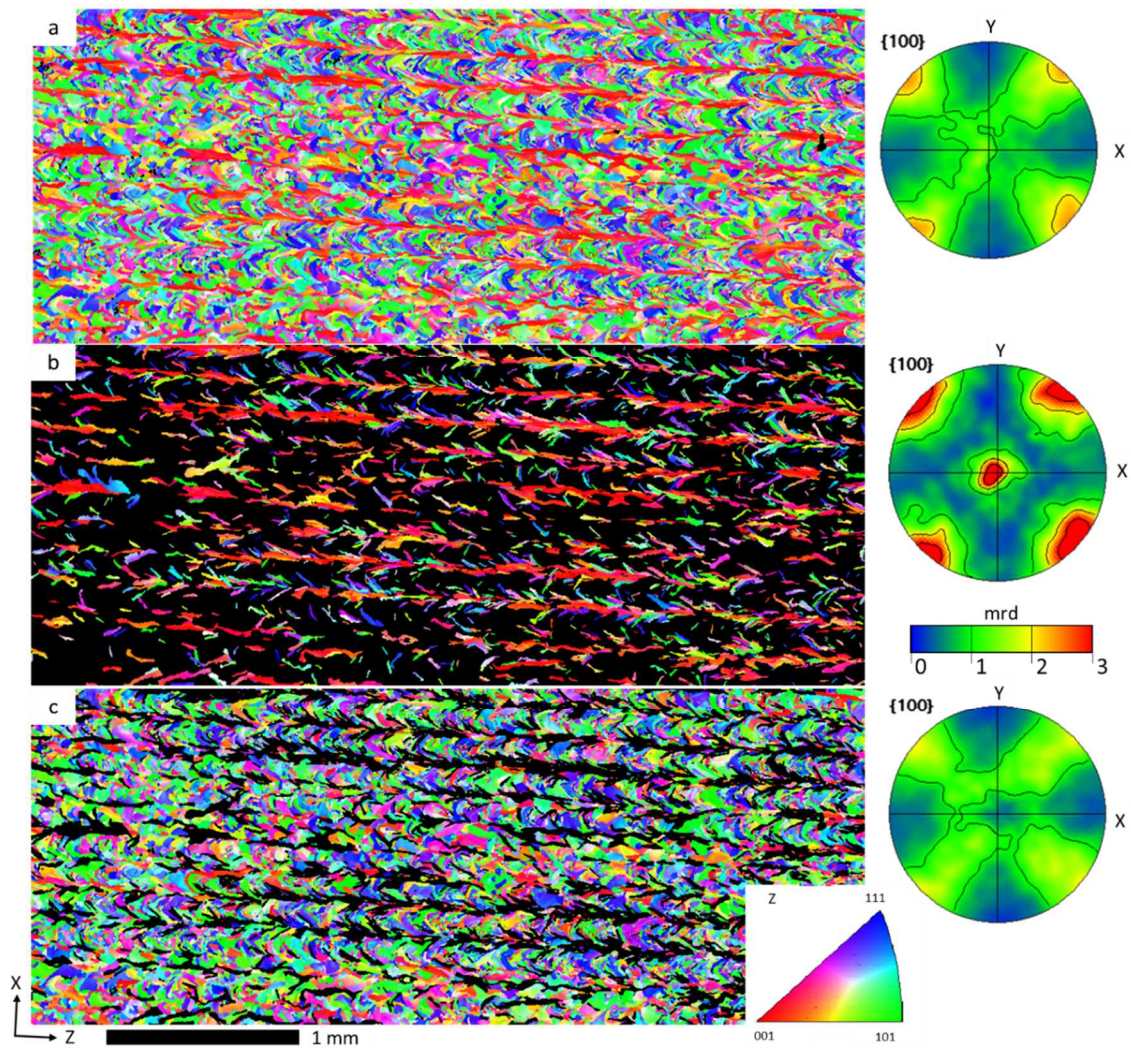


Figure 8. EBSD IPF maps and  $\langle 100 \rangle$  pole figures of the same area but with different sets of grains selected on a shape criterion: a) the whole grain population, b) elongated grains (aspect ratio  $> 4$ ) and c) the complementary set

### 3.3. Velocities of ultrasonic waves

Figure 9 and Figure 10 show examples of transient signals recorded in the case of longitudinal and transverse US waves, respectively. In the case of transverse waves, three different measurements are proposed to illustrate the signal variations with respect to polarization directions for a common propagation direction. We observe that the velocity of transverse waves is different for polarizations aligned with Y direction (slow shear mode) or Z direction (fast shear mode), the two types of waves coexisting for a polarization at  $45^\circ$  from Y axis. This results from the elastic anisotropy of the polycrystal and confirms the assumption considering that the three symmetry axes of the orthorhombic material are X, Y and Z.

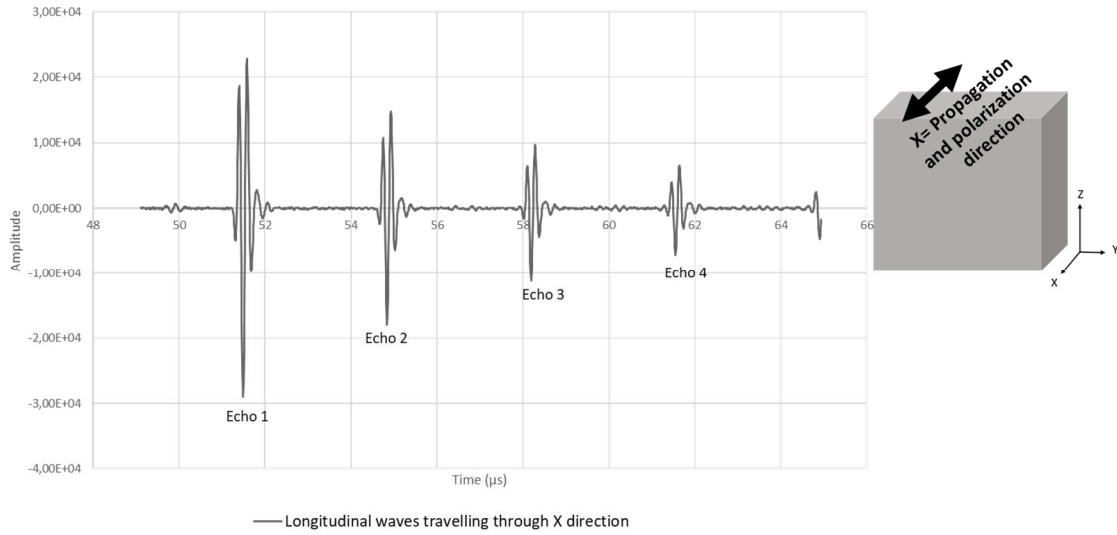


Figure 9. Acquisition signal obtained with immersed transducers in transmission mode in the X direction: only multiple echoes corresponding to longitudinal wave contributions can be observed

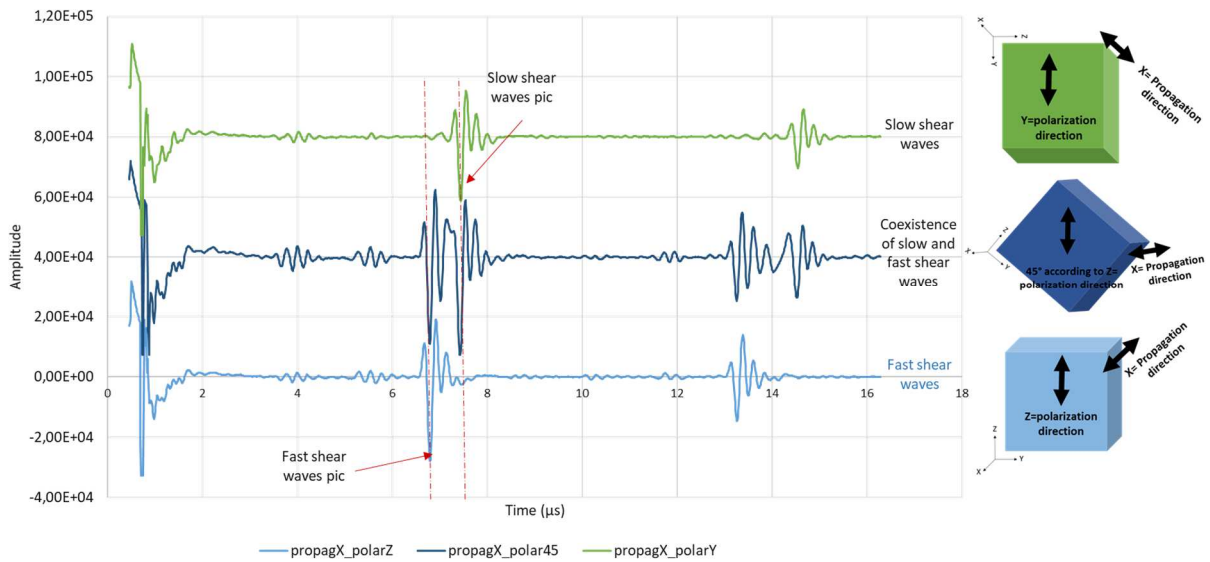


Figure 10. Acquisition signals obtained with shear contact transducers in transmission mode in the X direction: observation of transverse ultrasound wave generation for three different polarization directions with respect to the sample axis

Table 2 collects the velocities as a function of polarization directions and anisotropy factors calculated using equation (1). Longitudinal waves are slightly slower along the Z direction than along X and Y direction. Transverse waves along X and Y direction pointed out a significant anisotropy of velocities between Z and X (or Y) directions. Transverse waves polarized along Z direction have a higher velocity than those polarized along X or Y direction, leading to anisotropy factors of  $9.3 \pm 2.5\%$  and  $10 \pm 0.2\%$ , respectively. The higher uncertainty on  $\alpha_x$  is due to the smaller propagation distance in this direction. Although X and Y sample axes are equivalent with respect to lasing conditions, the value of  $\alpha_z$  is very low but not equal to 0, which could be due both to measurement errors or and to the difference between X and Y dimensions.

Table 2. Velocities and anisotropy factors measured for longitudinal and transverse US waves

Propagation directions	Velocity of longitudinal waves [m/s]	Transverse waves		
		polarization direction	velocity [m/s]	anisotropy factor (%)

X	5910	Y	2783	$\alpha_X = 9.3$	$\pm 2.5$
		Z	3054		
Y	5908	X	2762	$\alpha_Y = 10.0$	$\pm 0.2$
		Z	3054		
Z	5811	X	2995	$\alpha_Z = 1.1$	$\pm 0.2$
		Y	3028		

### 3.4. Anisotropy estimations from EBSD and wave velocity measurements

The Voigt, Reuss and Hill schemes can be used to evaluate the stiffness tensor of a polycrystal from its orientation distribution function and stiffness coefficients of the single crystal as an input. The orientation distribution function was extracted from the EBSD data of Figure 8 and the single-crystal stiffness coefficients are given in Table 1. As an example, the stiffness matrix expressed in the sample coordinates and obtained with the Hill model is given in Table 3a. It can be seen that the anisotropy is very close to elastic tetragonality (orthotropy where  $C_{11} = C_{22}$ ,  $C_{23} = C_{13}$ ,  $C_{44} = C_{55}$ ) but differs from transverse isotropy since  $C_{66} \neq (C_{11}-C_{12})/2$ . In a first approximation, this means that the polycrystal can be described by 6 coefficients. Some of these coefficients can be calculated assuming this tetragonal symmetry using the following equations [50,51]:

$$\text{Propagation along X: } V_{XY} = \sqrt{\frac{C_{66}}{\rho}}, \quad V_{XZ} = \sqrt{\frac{C_{55}}{\rho}} \quad (2)$$

$$\text{Propagation along Y: } V_{YX} = \sqrt{\frac{C_{66}}{\rho}}, \quad V_{YZ} = \sqrt{\frac{C_{44}}{\rho}} \quad (3)$$

$$\text{Propagation along Z: } V_{ZX} = \sqrt{\frac{C_{55}}{\rho}}, \quad V_{ZY} = \sqrt{\frac{C_{44}}{\rho}} \quad (4)$$

where  $\rho$  is the density of the material and  $V_{ij}$  is the velocity along direction  $i$  of a quasi-transverse wave polarized in direction  $j$ .

Table 3. a) Stiffness coefficients in GPa calculated from the texture of Figure 8.a and the single-crystal stiffness coefficients given at Table 1.a using a Hill model; b) stiffness matrix for an ideal orthotropic crystal

$$\text{a) } \begin{pmatrix} 294.15 & 126.61 & 135.94 & 0.4 & 0.5 & -2.42 \\ 126.61 & 294.49 & 135.6 & -0.4 & 1.15 & 2.36 \\ 135.94 & 135.6 & 285.17 & 0 & -1.65 & 0.07 \\ 0.4 & -0.4 & 0 & 81.66 & 0.08 & 1.1 \\ 0.5 & 1.15 & -1.65 & 0.08 & 82.02 & 0.39 \\ -2.42 & 2.36 & 0.07 & 1.1 & 0.39 & 72.98 \end{pmatrix} \quad \text{b) } \begin{pmatrix} C_{11} & C_{12} & C_{13} & 0 & 0 & 0 \\ C_{12} & C_{22} & C_{23} & 0 & 0 & 0 \\ C_{13} & C_{23} & C_{33} & 0 & 0 & 0 \\ 0 & 0 & 0 & C_{44} & 0 & 0 \\ 0 & 0 & 0 & 0 & C_{55} & 0 \\ 0 & 0 & 0 & 0 & 0 & C_{66} \end{pmatrix}$$

Therefore, it is possible to calculate the anisotropy factor,  $\alpha_i$  (equation 1,  $i=X, Y$  or  $Z$ ) in each propagation direction without to measure the material density (cf. Table 4). The calculated velocities vary qualitatively with the same trends as the measured ones. Ratio  $\alpha_Z$  is estimated lower than 0.25 whatever the mechanical model or the stiffness coefficient used. As expected,  $\alpha_X$  and  $\alpha_Y$  were close to each other. Table 4 gives the mean values of these values when calculated with three different mechanical models and each set of Inconel 625 single-crystal stiffness matrix reported in Table 1. These values are compared with the anisotropy factor measured by US propagation in the Y direction (this value was preferred to  $\alpha_X$  since the accuracy was found better in Y direction). It can be seen that calculated values are much lower than the measured one, whatever the model or the coefficients set. Calculations were also performed starting from others EBSD maps or from ODF (orientation distribution function) obtained by X-Ray diffraction. They all lead to similar anisotropy factors. This means that the model used here with representative crystallographic texture resulting from the AM process does not fully explain the magnitude of elastic anisotropy measured on the as-manufactured material.

Table 4. Mean values of anisotropy factors calculated along X and Y directions from the texture measurement, using three different mechanical models and two sets of single crystal stiffness coefficients.

	Voigt	Hill	Reuss
$C_{ij}$ from [41]	5,39	5,73	6,17
$C_{ij}$ from [42]	5,55	5,91	6,38
US propagation measurement along Y	10±0.2		
$C_{ij}$ computed in §4.2	7.84	8.42	9.59

## 4. Discussion

### 4.1. Mechanisms of the formation of the crystallographic texture

The crystallographic texture observed in the present work is clearly related to the building strategy. It is associated with the minor presence of elongated grains aligned along the Z (building) direction, with their  $\langle 100 \rangle$  directions parallel to the Z direction and to the two scanning directions of the laser beam. Moreover, it was noted that these grains are mostly located in the middle of successive ex-liquid pools. A similar texture have been also measured in another work [18]. These observations can be qualitatively explained on the basis of usual solidification mechanisms. In classical industrial casting processes, metals with a cubic symmetry are known to solidify through the development of dendrites -or cells- with their primary and secondary arms oriented along  $\langle 100 \rangle$  directions [52,53]. In the presence of a temperature gradient, dendrites with one  $\langle 100 \rangle$  direction close to the normal to the solidification front, i.e. parallel to the gradient, grow more rapidly than the others. The growth competition between dendrites can progressively lead to significant solidification textures, provided that the direction of the thermal gradient remains stable over sufficient distances. Nickel-based alloys are particularly sensitive to this mechanism, which is used to elaborate single-crystal components for aeronautic applications [54]. In the case of powder-bed additive manufacturing, although solidification rates are high, thermal gradients are high too and dendritic- or cellular- solidification still takes place [49,55]. This was confirmed in the present work by the observation of segregation cells (Figure 3.d). However, the selection of favorable crystal orientations is difficult, due to two specificities of the process: i) the size of one pool is too small to enable the selection mechanism to be effective during only one solidification step [56] and ii) the direction of normal to the thermal gradient changes at each deposition layer, due to more or less complex lasing strategies. Figure 11.a shows the typical shape of liquid pools associated with the melting of a metallic alloy by a moving laser beam [57,58]. This shape is often approximated by the so-called Rosenthal solution, developed for welding applications [59], which express the temperature distribution around a moving point heat source. Using this model, Pauza *et al.* pointed out that the elongation of the liquid pool in AM processes differ from an alloy to the other alloy, due the differences of thermal conductivities, solidification temperature range [28] or scanning strategy [60]. This is illustrated in Figure 11.b, where it is seen that the liquid pool is expected to be much elongated in case of nickel-based superalloys. Based on these considerations and on the lasing strategy used in the present work (cf. Figure 1), Figure 11.c symbolizes the evolution of the directions of thermal gradient at successive solidification fronts, for two locations with respect to the liquid pools (black and white arrows). Although this 2D representation is very schematic, it highlights the fact that the local thermal gradient rotates at each scanning layer, except for the grains growing in the middle of successive aligned liquid pools, for which the solidification direction remains approximatively parallel to the building direction. This can qualitatively explain why elongated  $\langle 100 \rangle$ -oriented grains can only develop at these locations. In their very recent paper, Pauza et al. obtained similar results on Inconel 718 alloy. They also inferred the same relations between texture and scanning strategy using a numerical approach based on a Monte Carlo Potts model [28]. It is likely that a misalignment between successive parallel lasing paths (ex. paths 1, 3 and 5 in Figure 11.c) may still reduce the magnitude of final elastic anisotropy in the material.

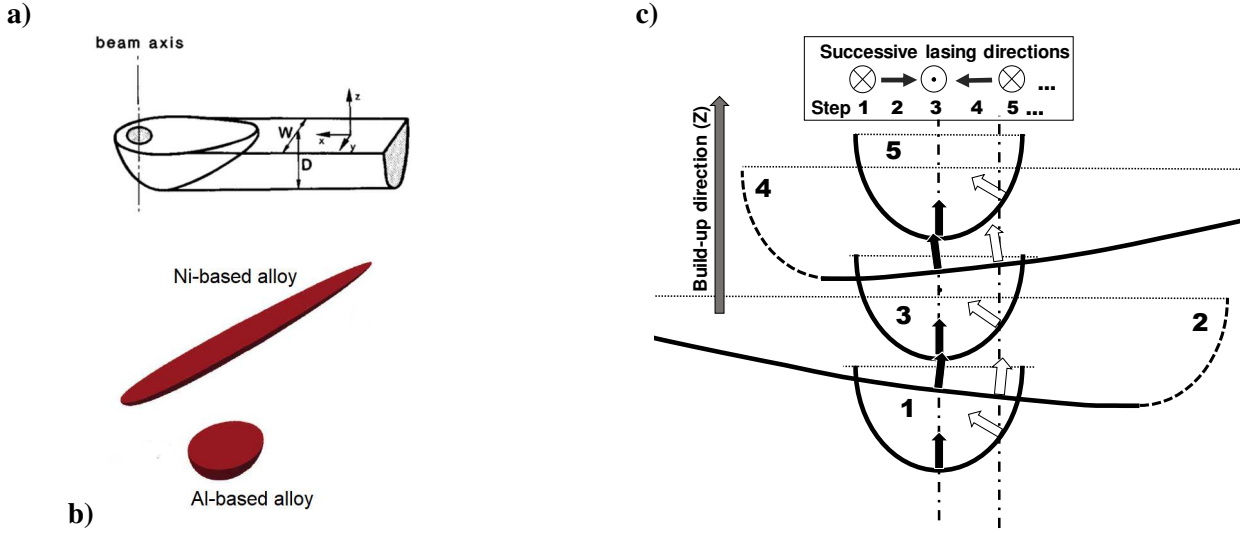


Figure 11. a) approximate shape of the liquid pool due to a moving laser beam (from [57]); b) elongation of the melting pool for two metallic alloys with different thermal properties (from [28]) ; c) schematic illustration of the variation of the direction of thermal gradient at two different places (black or white arrows) with respect to successive melting pools

#### 4.2. Relation between texture and velocities of ultrasonic waves

The difference between velocities measured along lasing plane directions (X, Y) and along the building direction Z is qualitatively but not quantitatively explained by the model used in the previous section. The parameters of the model include the crystallographic texture, the stiffness constants of the single crystal taken from the literature and the assumption of the Voigt, Hill or Reuss scheme.

As previously mentioned, textures evaluated at different localizations and with different techniques (EBSD and X-Ray Diffraction) led to similar results, meaning that the measurements can be assumed as representative enough. Concerning stiffness coefficients of the single crystal, only two sets, close to each other, were available. The experimental estimation of stiffness of single crystals is a difficult challenge, which could lead to values with rather low accuracy. The problem can be taken reversely: which cubic properties of the grain would at best reproduce the observed velocities, considering that the texture is known and that the Hill scheme can be used in a first approximation? To this aim, the parameter space  $C_{11}$ ,  $C_{12}$  and  $C_{44}$  has been discretized first with a coarse step of 2 GPa and then with a finer step of 0.2 GPa around the best solution. For each set of parameters, the stiffness matrix has been computed using the crystallographic texture and the Hill scheme.

The three elastic plane waves (one quasi-longitudinal wave, and two quasi-shear waves) were computed using SlowBaw program. To this aim, the elasto-dynamic equations within an anisotropic solid -assumed continuous and infinite- were solved [61]. When looking for plane waves solutions propagating in the solid, with a mathematical

expression  $\mathbf{u} = \hat{\mathbf{u}}F\left(t - \frac{\mathbf{n} \cdot \mathbf{x}}{V}\right)$ , where  $\mathbf{n}$  is a unitary vector,  $\hat{\mathbf{u}}$  the plane wave amplitude,  $V$  the phase velocity and

$F$  a general function, we are led to solve the Christoffel's equation (1) :

$$\sum_{l=1}^3 \Gamma_{il} \hat{u}_l = \rho V^2 \hat{u}_i, \quad i=1 \dots 3 \quad (5)$$

With  $\rho$  the mass density and  $\Gamma$  a second rank tensor defined by  $\Gamma_{il} = C_{ijkl} n_j n_k$  ( $C_{ijkl}$  is the elastic tensor). It results that the plane wave amplitude  $\hat{\mathbf{u}}$  solutions of Christoffel's equation are eigen vectors of  $\Gamma$  with the eigen values  $\gamma = \rho V^2$ .

The velocities were calculated for each set of elastic coefficients of the parameter space, using a mass density of  $8440 \text{ kg.m}^{-3}$ . The most representative set of coefficients was chosen by the least squares of the difference between the measured velocities and the calculated ones. The best coefficients found were then:

$$C_{11} = 226.6 \text{ GPa}, C_{12} = 162.6 \text{ GPa}, C_{44} = 134 \text{ GPa}.$$

The associated Zener factor  $A=4.1$  is much higher than the one obtained from [41,42], even than those found in the literature for different Ni-based alloys (between 2.5 and 3.5 [62]). This set of coefficients gives an  $\alpha_Y$  value of 8.6, which is closer to the measured value  $\alpha = 10$ . However, those coefficients still under-evaluate the observed experimental anisotropy.

Table 5: Velocities optimized using the measured texture, the Hill scheme and the SlowBaw program.

Propagation directions	Velocity of longitudinal waves [m/s]	Transverse waves		
		polarization direction	velocity [m/s]	anisotropy factor (%)
X	5932	Y	2781	$\alpha_X=8.6$
		Z	3030	
Y	5928	X	2778	$\alpha_Y=8.5$
		Z	3025	
Z	5791	X	3021	$\alpha_Z=0.3$
		Y	3030	

The second factor that can be considered is the model used to describe the anisotropy of the polycrystal. The Hill scheme is usually relevant for equiaxed grains, whereas in our material the grains are rather elongated in the building direction. To assess the effect of shape, let us consider two situations. First, a US wave propagating along the building direction. This situation corresponds better to the Voigt iso-strain model than the Hill scheme and would lead to stiffer behavior (upper bound). This agrees with our results since Hill approximation leads to under-evaluated longitudinal velocities along Z. Inversely, when a longitudinal wave along X or Y is considered, the stiffness is better evaluated by the Reuss model which corresponds to a lower bound. Again, this agrees with our result where the Hill approximation leads to over-evaluated longitudinal velocities in the X and Y directions.

Others microstructure features like internal defects could have a second order influence on the stiffness. In case of tensile-test properties such as maximum strength or elongation, the literature often does not arbitrate between the respective influences of crystallographic texture and internal defects, such as alignment of porosities or traces of oxide between successive layers. Although alignments of porosities have effectively been detected in our case (Figure 3), the very low volume fraction of these defects shall not affect the elastic properties of the AM material. No strong oxidation was evidenced at the investigation scales and with techniques used in the present work. Another source of propagation anisotropy could be the difference of grain size, i.e. of grain boundary density, pointed out by intercept measurement (cf. §.3.1).

Finally, it is important to remember that the ultrasonic measurements are incomplete and are based on a strong hypothesis which assumes that the X, Y, and Z directions are the symmetry axes of an orthotropic medium. This assumption can generate a significant bias, in particular for contact measurements of shear wave properties. More suitable measurements, without *a priori* assumption on the symmetry axes of the anisotropic material, could be tempted with more sophisticated US characterization setup, allowing a global identification of the stiffness tensor [63,64].

## 5. Conclusions:

The microstructure and texture anisotropies within an Inconel 625 component manufactured by laser powder bed fusion have been investigated, as well as their consequences on ultrasound wave propagation. From this work, the following conclusions can be drawn:

- The microstructure is composed of two types of grains: columnar grains, aligned along the build-up direction, develop in the middle of the melt pools. In between, grains appear less elongated and inclined relative to the build-up direction.
- The resulting crystallographic texture is low and corresponds to a rotated cube texture. Its main component is inherited from the columnar grains which  $\langle 100 \rangle$  directions are aligned with the build-up direction. The other grains form fibers around the two axes in the XY plane at  $45^\circ$  from X.
- The development of elongated textured grains is a result of the lasing strategy, in which the melt pools overlaps every two passes. As a consequence, the normal to the thermal gradient through the solidification front remains stable in the middle of successive melt pools, which drives the columnar growth together with the  $\langle 100 \rangle$  selection.
- The low texture has limited effect but still measurable on longitudinal waves propagation. However, the elastic anisotropy can be easily highlighted when transverse waves polarized along different directions are used.
- The difference detected between velocities of ultrasonic waves measured parallelly and perpendicularly to the build-up direction was qualitatively inferred from the crystallographic texture, using a homogenization model from single- to poly-crystal elastic properties.
- Inversely, this homogenization scheme was coupled with an optimization algorithm to re-evaluate the single crystal stiffness constants of the material.

**Acknowledgments :** This work was partly supported by the French Region Lorraine, through a dedicated research project between Université de Lorraine and CEA-Tech.

### Data Availability Statement

The raw/processed data required to reproduce these findings cannot be shared at this time due to technical or time limitations.

### 6. References:

- [1] W.E. Frazier, Metal Additive Manufacturing: A Review, *J. Mater. Eng. Perform.* 23 (2014) 1917–1928. <https://doi.org/10.1007/s11665-014-0958-z>.
- [2] Q. Jia, D. Gu, Selective laser melting additive manufacturing of Inconel 718 superalloy parts: Densification, microstructure and properties, *J. Alloys Compd.* 585 (2014) 713–721. <https://doi.org/10.1016/j.jallcom.2013.09.171>.
- [3] S. Shao, M.M. Khonsari, S. Guo, W.J. Meng, N. Li, Overview: Additive Manufacturing Enabled Accelerated Design of Ni-based Alloys for Improved Fatigue Life, *Addit. Manuf.* 29 (2019) 100779. <https://doi.org/10.1016/j.addma.2019.100779>.
- [4] K.N. Amato, S.M. Gaytan, L.E. Murr, E. Martinez, P.W. Shindo, J. Hernandez, S. Collins, F. Medina, Microstructures and mechanical behavior of Inconel 718 fabricated by selective laser melting, *Acta Mater.* 60 (2012) 2229–2239. <https://doi.org/10.1016/j.actamat.2011.12.032>.
- [5] S. Bremen, W. Meiners, K. Wissenbach, R. Poprawe, Correlation of the High Power SLM Process with Resulting Material Properties for IN718, *BHM Berg- Hüttenmänn. Monatshefte.* 162 (2017) 179–187. <https://doi.org/10.1007/s00501-017-0589-4>.
- [6] S.K. Everton, M. Hirsch, P. Stravroulakis, R.K. Leach, A.T. Clare, Review of in-situ process monitoring and in-situ metrology for metal additive manufacturing, *Mater. Des.* 95 (2016) 431–445. <https://doi.org/10.1016/j.matdes.2016.01.099>.

- [7] Y. Kok, X.P. Tan, P. Wang, M.L.S. Nai, N.H. Loh, E. Liu, S.B. Tor, Anisotropy and heterogeneity of microstructure and mechanical properties in metal additive manufacturing: A critical review, *Mater. Des.* 139 (2018) 565–586. <https://doi.org/10.1016/j.matdes.2017.11.021>.
- [8] D. Deng, R.L. Peng, H. Brodin, J. Moverare, Microstructure and mechanical properties of Inconel 718 produced by selective laser melting: Sample orientation dependence and effects of post heat treatments, *Mater. Sci. Eng. A.* 713 (2018) 294–306. <https://doi.org/10.1016/j.msea.2017.12.043>.
- [9] T. Bauer, K. Dawson, A.B. Spierings, K. Wegener, Microstructure and mechanical characterisation of SLM processed Haynes® 230®, in: *Proc. 26th Annu. Int. Solid Free. Fabr. Symp., Laboratory for Freeform Fabrication and University of Texas at Austin*, 2015: pp. 813–822. <https://doi.org/10.3929/ethz-a-010584903>.
- [10] Z. Wang, K. Guan, M. Gao, X. Li, X. Chen, X. Zeng, The microstructure and mechanical properties of deposited-IN718 by selective laser melting, *J. Alloys Compd.* 513 (2012) 518–523. <https://doi.org/10.1016/j.jallcom.2011.10.107>.
- [11] E. Chlebus, K. Gruber, B. Kuźnicka, J. Kurzac, T. Kurzynowski, Effect of heat treatment on the microstructure and mechanical properties of Inconel 718 processed by selective laser melting, *Mater. Sci. Eng. A.* 639 (2015) 647–655. <https://doi.org/10.1016/j.msea.2015.05.035>.
- [12] L.E. Criales, Y.M. Arisoy, B. Lane, S. Moylan, A. Donmez, T. Özel, Laser powder bed fusion of nickel alloy 625: Experimental investigations of effects of process parameters on melt pool size and shape with spatter analysis, *Int. J. Mach. Tools Manuf.* 121 (2017) 22–36. <https://doi.org/10.1016/j.ijmachtools.2017.03.004>.
- [13] E.A. Lass, M.R. Stoudt, M.E. Williams, M.B. Katz, L.E. Levine, T.Q. Phan, T.H. Gnaeupel-Herold, D.S. Ng, Formation of the Ni<sub>3</sub>Nb δ-Phase in Stress-Relieved Inconel 625 Produced via Laser Powder-Bed Fusion Additive Manufacturing, *Metall. Mater. Trans. A.* 48 (2017) 5547–5558. <https://doi.org/10.1007/s11661-017-4304-6>.
- [14] M. Rombouts, G. Maes, M. Mertens, W. Hendrix, Laser metal deposition of Inconel 625: Microstructure and mechanical properties, *J. Laser Appl.* 24 (2012) 052007. <https://doi.org/10.2351/1.4757717>.
- [15] T. Etter, K. Kunze, F. Geiger, H. Meidani, Reduction in mechanical anisotropy through high temperature heat treatment of Hastelloy X processed by Selective Laser Melting (SLM), *IOP Conf. Ser. Mater. Sci. Eng.* 82 (2015) 012097. <https://doi.org/10.1088/1757-899X/82/1/012097>.
- [16] B. AlMangour, D. Grzesiak, J.-M. Yang, Scanning strategies for texture and anisotropy tailoring during selective laser melting of TiC/316L stainless steel nanocomposites, *J. Alloys Compd.* 728 (2017) 424–435. <https://doi.org/10.1016/j.jallcom.2017.08.022>.
- [17] H. Helmer, A. Bauereiß, R.F. Singer, C. Körner, Grain structure evolution in Inconel 718 during selective electron beam melting, *Mater. Sci. Eng. A.* 668 (2016) 180–187. <https://doi.org/10.1016/j.msea.2016.05.046>.
- [18] O. Andreau, I. Koutiri, P. Peyre, J.-D. Penot, N. Saintier, E. Pessard, T. De Terris, C. Dupuy, T. Baudin, Texture control of 316L parts by modulation of the melt pool morphology in selective laser melting, *J. Mater. Process. Technol.* 264 (2019) 21–31. <https://doi.org/10.1016/j.jmatprotec.2018.08.049>.
- [19] Z. Sun, X. Tan, S.B. Tor, C.K. Chua, Simultaneously enhanced strength and ductility for 3D-printed stainless steel 316L by selective laser melting, *NPG Asia Mater.* 10 (2018) 127–136. <https://doi.org/10.1038/s41427-018-0018-5>.
- [20] R.R. Dehoff, M.M. Kirka, W.J. Sames, H. Bilheux, A.S. Tremsin, L.E. Lowe, S.S. Babu, Site specific control of crystallographic grain orientation through electron beam additive manufacturing, *Mater. Sci. Technol.* 31 (2015) 931–938. <https://doi.org/10.1179/1743284714Y.0000000734>.
- [21] N. Nadammal, S. Cabeza, T. Mishurova, T. Thiede, A. Kromm, C. Seyfert, L. Farahbod, C. Haberland, J.A. Schneider, P.D. Portella, G. Bruno, Effect of hatch length on the development of microstructure, texture and

- residual stresses in selective laser melted superalloy Inconel 718, *Mater. Des.* 134 (2017) 139–150. <https://doi.org/10.1016/j.matdes.2017.08.049>.
- [22] A. Leicht, U. Klement, E. Hryha, Effect of build geometry on the microstructural development of 316L parts produced by additive manufacturing, *Mater. Charact.* 143 (2018) 137–143. <https://doi.org/10.1016/j.matchar.2018.04.040>.
- [23] J.J.H. Lim, A.R.C. Malheiros, G. Bertali, C.J. Long, P.D. Freyer, M.G. Burke, Comparison of Additive Manufactured and Conventional 316L Stainless Steels, *Microsc. Microanal.* 21 (2015) 467–468. <https://doi.org/10.1017/S143192761500313X>.
- [24] B. AlMangour, D. Grzesiak, J.-M. Yang, Rapid fabrication of bulk-form TiB<sub>2</sub>/316L stainless steel nanocomposites with novel reinforcement architecture and improved performance by selective laser melting, *J. Alloys Compd.* 680 (2016) 480–493. <https://doi.org/10.1016/j.jallcom.2016.04.156>.
- [25] R. Muñoz-Moreno, V.D. Divya, S.L. Driver, O.M.D.M. Messé, T. Illston, S. Baker, M.A. Carpenter, H.J. Stone, Effect of heat treatment on the microstructure, texture and elastic anisotropy of the nickel-based superalloy CM247LC processed by selective laser melting, *Mater. Sci. Eng. A.* 674 (2016) 529–539. <https://doi.org/10.1016/j.msea.2016.06.075>.
- [26] V.A. Popovich, E.V. Borisov, A.A. Popovich, V.Sh. Sufiiarov, D.V. Masaylo, L. Alzina, Impact of heat treatment on mechanical behaviour of Inconel 718 processed with tailored microstructure by selective laser melting, *Mater. Des.* 131 (2017) 12–22. <https://doi.org/10.1016/j.matdes.2017.05.065>.
- [27] T.M. Rodgers, J.D. Madison, V. Tikare, Simulation of metal additive manufacturing microstructures using kinetic Monte Carlo, *Comput. Mater. Sci.* 135 (2017) 78–89. <https://doi.org/10.1016/j.commatsci.2017.03.053>.
- [28] J.G. Pauza, W.A. Tayon, A.D. Rollett, Computer Simulation of Microstructure Development in Powder-Bed Additive Manufacturing with Crystallographic Texture, *Be Submitt.* (2020).
- [29] M.J.P. Musgrave, *Crystal acoustics: Introduction to the Study of Elastic Waves and Vibrations in Crystals*, Acoustical Society of America, Holden-Day, 1970.
- [30] D. Royer, E. Dieulesaint, *Elastic Waves in Solids I: Free and Guided Propagation*, Springer-Verlag, Berlin Heidelberg, 2000. <http://www.springer.com/de/book/9783540659327>.
- [31] A. Lhémy, P. Calmon, I. Lecœur-Taïbi, R. Raillon, L. Paradis, Modeling tools for ultrasonic inspection of welds, *NDT E Int.* 33 (2000) 499–513. [https://doi.org/10.1016/S0963-8695\(00\)00021-9](https://doi.org/10.1016/S0963-8695(00)00021-9).
- [32] B. Chassignole, R. El Guerjouma, M.-A. Ploix, T. Fouquet, Ultrasonic and structural characterization of anisotropic austenitic stainless steel welds: Towards a higher reliability in ultrasonic non-destructive testing, *NDT E Int.* 43 (2010) 273–282. <https://doi.org/10.1016/j.ndteint.2009.12.005>.
- [33] G.D. Connolly, M.J.S. Lowe, J. a. G. Temple, S.I. Rokhlin, Correction of ultrasonic array images to improve reflector sizing and location in inhomogeneous materials using a ray-tracing model, *J. Acoust. Soc. Am.* 127 (2010) 2802–2812. <https://doi.org/10.1121/1.3372724>.
- [34] Q.Y. Lu, C.H. Wong, Applications of non-destructive testing techniques for post-process control of additively manufactured parts, *Virtual Phys. Prototyp.* 12 (2017) 301–321. <https://doi.org/10.1080/17452759.2017.1357319>.
- [35] R.J. Arts, P.N.J. Rasolofosaon, B.E. Zinszner, Complete inversion of the anisotropic elastic tensor in rocks: Experiment versus theory, in: *SEG Tech. Program Expand. Abstr.* 1991, Society of Exploration Geophysicists, 1991: pp. 1538–1541. <https://doi.org/10.1190/1.1888996>.
- [36] N. Leymarie, C. Aristégui, B. Audoin, S. Baste, Identification of complex stiffness tensor from waveform reconstruction, *J. Acoust. Soc. Am.* 111 (2002) 1232–1244. <https://doi.org/10.1121/1.1451072>.

- [37] M.-A. Ploix, P. Guy, B. Chassignole, J. Moysan, G. Corneloup, R.E. Guerjouna, Measurement of ultrasonic scattering attenuation in austenitic stainless steel welds: Realistic input data for NDT numerical modeling, *Ultrasonics*. 54 (2014) 1729–1736. <https://doi.org/10.1016/j.ultras.2014.04.005>.
- [38] R.G. Leisure, F.A. Willis, Resonant ultrasound spectroscopy, *J. Phys. Condens. Matter*. 9 (1997) 6001–6029. <https://doi.org/10.1088/0953-8984/9/28/002>.
- [39] A. Khabouchi, A. Hazotte, L. Germain, J.-D. Penot, L. Ducouso-Ganjehi, B. Marchand, B. Vayre, Relation between microstructure/texture anisotropy and ultrasound propagation in a Ni-based superalloy elaborated by laser powder bed fusion, in: Metz, France, 2017.
- [40] B. Beausir, J.-J. Fundenberger, ATEX, Université de Lorraine, Metz, 2017. [www.atex-software.eu](http://www.atex-software.eu).
- [41] Z. Wang, A.D. Stoica, D. Ma, A.M. Beese, Diffraction and single-crystal elastic constants of Inconel 625 at room and elevated temperatures determined by neutron diffraction, *Mater. Sci. Eng. A*. 674 (2016) 406–412. <https://doi.org/10.1016/j.msea.2016.08.010>.
- [42] T.M. Holden, R.A. Holt, A.P. Clarke, Intergranular strains in Inconel-600 and the impact on interpreting stress fields in bent steam-generator tubing, *Mater. Sci. Eng. A*. 246 (1998) 180–198. [https://doi.org/10.1016/S0921-5093\(97\)00732-6](https://doi.org/10.1016/S0921-5093(97)00732-6).
- [43] C. Zener, Contributions to the Theory of Beta-Phase Alloys, *Phys. Rev.* 71 (1947) 846–851. <https://doi.org/10.1103/PhysRev.71.846>.
- [44] A. Reuss, Berechnung der Fließgrenze von Mischkristallen auf Grund der Plastizitätsbedingung für Einkristalle., *ZAMM - J. Appl. Math. Mech. Z. Für Angew. Math. Mech.* 9 (1929) 49–58. <https://doi.org/10.1002/zamm.19290090104>.
- [45] W. Voigt, *Lehrbuch der Kristallphysik*, in: B. B. Teubner, Leipzig, 1928: p. 739.
- [46] R. Hill, The Elastic Behaviour of a Crystalline Aggregate, *Proc. Phys. Soc. Sect. A*. 65 (1952) 349–354. <https://doi.org/10.1088/0370-1298/65/5/307>.
- [47] M. Tang, P.C. Pistorius, J.L. Beuth, Prediction of lack-of-fusion porosity for powder bed fusion, *Addit. Manuf.* 14 (2017) 39–48. <https://doi.org/10.1016/j.addma.2016.12.001>.
- [48] G. Marchese, S. Parizia, M. Rashidi, A. Saboori, D. Manfredi, D. Ugues, M. Lombardi, E. Hryha, S. Biamino, The role of texturing and microstructure evolution on the tensile behavior of heat-treated Inconel 625 produced via laser powder bed fusion, *Mater. Sci. Eng. A*. 769 (2020) 138500. <https://doi.org/10.1016/j.msea.2019.138500>.
- [49] G. Boussinot, M. Apel, J. Zielinski, U. Hecht, J.H. Schleifenbaum, Strongly Out-of-Equilibrium Columnar Solidification During Laser Powder-Bed Fusion in Additive Manufacturing, *Phys. Rev. Appl.* 11 (2019) 014025. <https://doi.org/10.1103/PhysRevApplied.11.014025>.
- [50] W.P. Mason, *Physical acoustics and the properties of solids.*, Van Nostrand, Princeton, N.J., 1958. <https://catalog.hathitrust.org/Record/001479862>.
- [51] W.C. Van Buskirk, S.C. Cowin, R.N. Ward, Ultrasonic Measurement of Orthotropic Elastic Constants of Bovine Femoral Bone, *J. Biomech. Eng.* 103 (1981) 67–72. <https://doi.org/10.1115/1.3138262>.
- [52] J.A. Dantzig, M. Rappaz, *Solidification - 2nd Edition*, EPFL PRESS, 2016. <https://www.epflpress.org/product/501/9782889142071/solidification>.
- [53] W. W. Kurz, D.J. Fisher, *Fundamentals of Solidification*, Trans Tech Publications, 1998. [/book/fundamentals-of-solidification/978-3-0357-3239-9](https://www.trans-tech.com/book/fundamentals-of-solidification/978-3-0357-3239-9).
- [54] A.F. Giamei, Development of Single Crystal Superalloys: A Brief History, *Adv. Mater. Process.* (2013) 26–30.

- [55] Y.M. Arisoy, L.E. Criales, T. Özel, B. Lane, S. Moylan, A. Donmez, Influence of scan strategy and process parameters on microstructure and its optimization in additively manufactured nickel alloy 625 via laser powder bed fusion, *Int. J. Adv. Manuf. Technol.* 90 (2017) 1393–1417. <https://doi.org/10.1007/s00170-016-9429-z>.
- [56] Y. Li, A. Olmedilla, M. Založnik, J. Zollinger, L. Dembinski, A. Mathieu, Solidification microstructure during selective laser melting of Ni based superalloy: experiment and mesoscopic modelling, *IOP Conf. Ser. Mater. Sci. Eng.* 529 (2019) 012004. <https://doi.org/10.1088/1757-899X/529/1/012004>.
- [57] M. Gremaud, M. Carrard, W. Kurz, The microstructure of rapidly solidified Al-Fe alloys subjected to laser surface treatment, *Acta Metall. Mater.* 38 (1990) 2587–2599. [https://doi.org/10.1016/0956-7151\(90\)90271-H](https://doi.org/10.1016/0956-7151(90)90271-H).
- [58] N.J. Harrison, I. Todd, K. Mumtaz, Reduction of micro-cracking in nickel superalloys processed by Selective Laser Melting: A fundamental alloy design approach, *Acta Mater.* 94 (2015) 59–68. <https://doi.org/10.1016/j.actamat.2015.04.035>.
- [59] D. Rosenthal, Mathematical Theory of Heat Distribution during Welding and Cutting, *Weld. J.* 20 (1941) 220–234.
- [60] L.E. Criales, Y.M. Arisoy, B. Lane, S. Moylan, A. Donmez, T. Özel, Predictive modeling and optimization of multi-track processing for laser powder bed fusion of nickel alloy 625, *Addit. Manuf.* 13 (2017) 14–36. <https://doi.org/10.1016/j.addma.2016.11.004>.
- [61] V. Laude, *Phononic Crystals: Artificial Crystals for Sonic, Acoustic, and Elastic Waves*, De Gruyter, 2015. <https://www.degruyter.com/view/title/300496>.
- [62] S.I. Ranganathan, M. Ostoja-Starzewski, Universal Elastic Anisotropy Index, *Phys. Rev. Lett.* 101 (2008) 055504. <https://doi.org/10.1103/PhysRevLett.101.055504>.
- [63] C. Aristégui, S. Baste, Optimal recovery of the elasticity tensor of general anisotropic materials from ultrasonic velocity data, *J. Acoust. Soc. Am.* 101 (1997) 813–833. <https://doi.org/10.1121/1.418040>.
- [64] S.I. Rokhlin, T.K. Bolland, L. Adler, Reflection and refraction of elastic waves on a plane interface between two generally anisotropic media, *J. Acoust. Soc. Am.* 79 (1986) 906–918. <https://doi.org/10.1121/1.393764>.